UC Irvine
UC Irvine Previously Published Works

Title

Feasibility of photoacoustic-guided ultrasound treatment for port wine stains

Permalink

Journal

ISSN

Authors

Chua, Chloe J
Pandey, Prabodh K
Kelly, Kristen M
et al.

Publication Date

DOI

BASIC SCIENCE

Feasibility of photoacoustic-guided ultrasound treatment for port wine stains

Chloe J. Chua BS Candidate[1] | Prabodh K. Pandey PhD[2] | Kristen M. Kelly MD[3,4] | Liangzhong Xiang PhD[1,2,4]

[1]Department of Biomedical Engineering, University of California, Irvine, California, USA

[2]Department of Radiological Sciences, University of California, Irvine, California, USA

[3]Department of Dermatology, University of California, Irvine, California, USA

[4]Beckman Laser Institute, University of California, Irvine, California, USA

Correspondence

Liangzhong Xiang, PhD, Department of Biomedical Engineering, University of California, 825 Health Sciences Rd, Medical Sciences B, Room #134, Irvine, CA 92617, USA.
Email: liangzhx@uci.edu

Prabodh K. Pandey, PhD, Department of Radiological Sciences, University of California, 835 Health Sciences Rd, Irvine Hall, Room #132, Irvine, CA 92617, USA.
Email: pkpandey@hs.uci.edu

Abstract

Background and Objectives: Port wine birthmark, also known as port wine stain (PWS) is a skin discoloration characterized by red/purple patches caused by vascular malformation. PWS is typically treated by using lasers to destroy abnormal blood vessels. The laser heating facilitates selective photothermolysis of the vessels and attenuates quickly in the tissue due to high optical scattering. Therefore, residual abnormal capillaries deep in the tissue survive and often lead to the resurgence of PWS. Ultrasound (US) has also been proposed to treat PWS, however, it is nonselective with respect to the vasculature but penetrates deeper into the tissue. We aim to study the feasibility of a hybrid PWS treatment modality combining the advantages of both modalities.

Materials and Methods: In this manuscript, we propose a photoacoustic (PA) guided US focusing methodology for PWS treatment which combines the optical contrast-based selectivity with US penetration to focus the US energy onto the vasculature. The PA signals collected by the transducers, when time-reversed, amplified, and transmitted, converge onto the PWS, thus minimally affecting the neighboring tissue. We performed two- and three-dimensional simulations that mimic realistic transducers and medium properties in this proof of concept study.

Results: The time-reversed PA signals when transmitted from the transducers converged onto the vasculature, as expected, thus reducing the heating of the neighboring tissue. We observed that while the US focus is indeed affected due to experimental factors such as limited-view, large detector separation and finite detection bandwidth, and so forth, the US did focus completely or partially onto the vasculature demonstrating the feasibility of the proposed methodology.

Conclusion: The results demonstrate the potential of the proposed methodology for PWS treatment. This treatment method can destroy the deeper capillaries while minimally heating the neighboring tissue, thus reducing the chances of the resurgence of PWS and as well as cosmetic scarring.

KEYWORDS

photoacoustic (PA)-guided ultrasound (US), photoacoustics (PA), port wine stain (PWS), time-reversal (TR), high-intensity focused ultrasound (HIFU)

INTRODUCTION

Port wine stain (PWS), a skin discoloration characterized by deep red or purple patches, represents the second most common congenital vascular malformation affecting 3−5 in every 1000 infants born.[1] PWS often darkens over time and potentially become nodular or hypertrophic when left untreated.[1] Previous therapeutic methods for treating PWS include surgical excision, freezing, tattooing, and radiation therapy.[2] These methods did not produce satisfactory results and often caused cosmetic scarring.[2] Thus, these methods are outdated and no longer practiced.

Chloe J. Chua and Prabodh K. Pandey contributed equally to this study.

Introduced in the 1970s, Argon laser treatment was one of the first effective approaches to PWS therapy.[3] The argon laser emits blue-green light between 488 and 514 nm, which is absorbed more readily by hemoglobin in PWS blood vessels.[4] As a result of absorbing radiant energy, the vessels heat up, causing thrombosis and destruction.[2] However, it can irreversibly damage the epidermis due to unwanted absorption by melanin.[4] In 1983, the concept of selective photothermolysis was presented[5] in which the laser wavelength is carefully chosen based on the target chromophore to achieve photon absorption and target heating, while neighboring tissues are mostly unaffected, thus reducing negative consequences such as scarring and dyspigmentation.[4]

Since the 1980s, PWS birthmarks are commonly treated using the pulsed-dye laser (PDL) in conjunction with epidermal cooling.[6,7] Pulsed dye lasers operating at 577−600 nm wavelengths are preferentially absorbed by hemoglobin in the PWS blood vessels causing thermal damage and thrombosis.[6,8] Nonetheless, PDLs have their shortcomings. The penetration depth of PDLs in tissue is limited due to high optical scattering and hence deeper capillaries remain untreated after the PDL therapy.[9] These untreated capillaries lead to the growth of new capillaries and hence the resurgence of PWS. Furthermore, increasing the intensity to generate larger vascular damage has the potential to cause dyspigmentation, especially in dark-skinned patients who have more epidermal melanin and reactive fibroblast responses.[10] The more melanin present, the more likely it is that melanin will absorb the energy and compete with other chromophores, lowering the treatment's efficacy. Furthermore, efficiently cooling the skin surface (cryogen spray, cold air, cooled gel, ice packs) is necessary to reduce pain during treatment[10] and avoid adverse effects.

Photodynamic therapy (PDT) as a vascular-targeted method for PWS treatment has shown to be potentially effective.[11-13] PDT is a treatment technique that combines a photosensitizer (typically injected intravenously) with light and oxygen to trigger a photochemical reaction that produces highly reactive singlet oxygen molecules that can cause cell death through apoptosis, necrosis, or autophagy.[11] The treatment can damage vascular endothelial cells selectively, coagulate blood vessels, cause fibrosis, and facilitate the removal of the skin's distorted enlarged capillary network.[12,13] However, there are risks of infection, thick scabs, and scar formation due to excessive PDT sessions or improper postoperative care.[14] Moreover, phototoxicity (due to the photosensitizer drug) can cause short and long-term side effects such as blisters and pigmentary change.[15]

According to a 2019 peer-reviewed article with 65 studies comprising 6207 PWS patients, only 21% of patients experienced 75%−100% of skin clearance.[16] In spite of significant technological advancements and pharmacological therapies, the efficacy of PWS therapy has not increased in recent years. Across the 65 studies spanning the past three decades, there was no evidence of any upward trend in mean clearance over time.[16] Although new technologies enter and mature the clinical setting, the proportion of patients with 75%−100% clearance has not increased. In summary, only a few studies in the last 30 years have been able to match or exceed the findings reported in the 1980s and early 1990s with the 577 and 585 nm PDLs.[16]

Ultrasound (US) waves have been demonstrated to be effective in treating a variety of wounds and PWS. Therapeutic US is a physical way of delivering nonionizing radiation into the tissues in the form of mechanical sound waves, which cause tissue heating.[17,18] The key advantages of US wound treatment include deep penetration into the wound and minimal risk of negative effects.[17] US is a frequently-used modality to image PWS lesions,[19,20] yet very little literature can be found on using US as a therapeutic treatment for PWS. In 2020, Kwiek et al.[21] utilized high-intensity focused US (HIFU) treatment to improve soft tissue hypertrophy which can be associated with PWS. The most notable shortcoming regarding US therapy for PWS treatment is the lack of selectivity. US therapy does not differentiate PWS-affected vasculature from surrounding healthy tissue, resulting in the entire area being irradiated. To prevent this issue, a new technique is needed to target aberrant vasculature.

Absorption of pulsed optical excitation in soft tissues is followed by thermoelastic expansion of the irradiated volume and subsequent production of US. This phenomenon is known as the photoacoustic (PA) effect.[22] The US waves thus generated can be sensed using ultrasonic transducers and the collected signals can be further processed to facilitate structural and functional imaging.[23–26] Over the past two decades, PA imaging has been widely explored for diagnostic imaging[27,28] and non-destructive material evaluation.[29,30]

Several past studies utilized PA guidance for US focusing.[31-33] However, these studies used the PA guidance to focus the US onto a focal point. The time-reversal-based focusing as demonstrated in this manuscript facilitates US focusing onto the optical absorption map. The proposed strategy could also be used with the existing methodology of US sonication using microbubbles for rupturing blood vessels,[34-36] as well as for improving permeability for intravascular delivery of gene therapy and medications.[37] This methodology can also assist other targeted US therapeutic techniques aimed at wound healing and cancer therapy.[38-41]

In this manuscript, we propose a novel treatment technique for PWS treatment that utilizes PA-guided US to focus onto the blood vessels. The PWS when excited by a pulsed laser generates PA waves, which can be sensed using ultrasonic transducers placed around the diseased tissue. These PA signals carry information about the location and shape of the vasculature. These
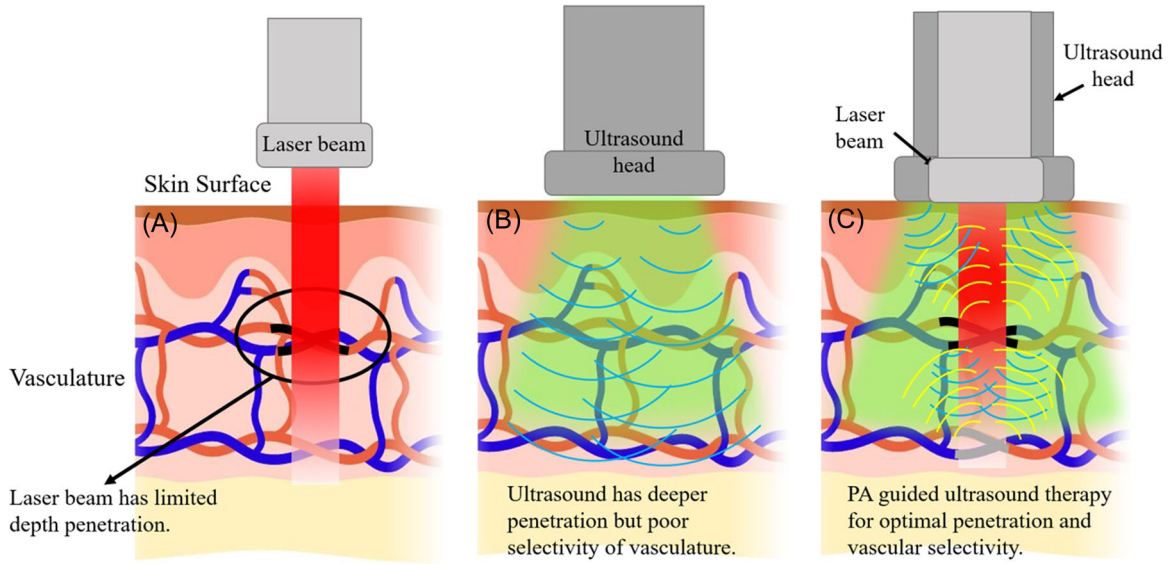
FIGURE 1 Schematic diagrams of (A) laser beam treatment, (B) US treatment, and (C) the proposed PA guided US therapy with optimal benefits. Yellow wavefronts: PA waves sensed by the transducers; Blue wavefronts: US transmitted by the transducers. PA, photoacoustic; US, ultrasound.

PA signals, when time-reversed, amplified, and transmitted from the transducers, converge the US energy onto the PWS itself, sparing the healthy neighboring tissues. Figure 1 demonstrates the schematics of purely optical and US-based treatment, along with the methodology proposed in this manuscript. We provide the theory behind PA and time-reversal in Section 2. Numerical studies performed are detailed in Section 3 and results are discussed in Section 4. Concluding remarks are offered in Section 5.

THEORY

The generation of PA waves following optical energy deposition (OED) in the tissue under the assumptions of thermal confinement and zero acoustic attenuation is based on the PA equation[42]:

$$\frac{\partial^2 p(\vec{r}, t)}{\partial t^2} - v^2 \nabla^2 p(\vec{r}, t) = \Gamma H(\vec{r}) \frac{\partial \delta(t)}{\partial t}, \quad (1)$$

where $\Gamma (= v^2 \beta / C_p)$ is the Gruneisen parameter, v is the speed of sound, β is the volumetric expansion coefficient, C_p is the specific heat at constant pressure, and H is the OED distribution. The pressure fields $p(\vec{r}, t)$ can be sensed using ultrasonic transducers placed on a detection grid around the region of interest till time T, long enough to ensure that the pressure fields vanish at each of the detectors for t > T.

The impulse response of acoustic detection h^{AD} is the pressure signal sensed by a detector due to a Dirac delta source located at $\vec{r}_0$ can be expressed as

$$h^{AD}(\vec{r}_0, t) = \int_S G(\vec{r}, t; \vec{r}_0, t) W(\vec{r}) d\vec{r} \quad (2)$$

with $G(\vec{r}, t; \vec{r}_0, t)$ being the Green's function corresponding to Equation 1, representing the pressure field at $\vec{r}$ due to the Dirac source located at $\vec{r}_0$ and $W(\vec{r})$ being the detector apodization.[43] The integral in Equation 2 represents the weighted integral over the transducer surface. Similarly, the impulse response of acoustic transmission h^{AT} is the pressure field at $\vec{r}_0$ due to Dirac delta transmission sources on the transducer surface and can be expressed as:

$$h^{AT}(\vec{r}_0, t) = \int_S G(\vec{r}_0, t; \vec{r}, t) W(\vec{r}) d\vec{r} \quad (3)$$

with $G(\vec{r}_0, t; \vec{r}, t)$ being the Green's function corresponding to Equation 1, representing the pressure field at $\vec{r}_0$ due to the Dirac source located at $\vec{r}$. Using the reciprocity theorem, we conclude that the detection and transmission impulse responses are the same, that is, $h^{AT}(\vec{r}_0, t) = h^{AD}(\vec{r}_0, t) = h^A(\vec{r}_0, t)$.

The pressure signal collected at the ith detector, located at $\vec{r}_i$ due to a pressure source at $\vec{r}_0$ can be expressed as the convolution (denoted by * sign) between the electrical and acoustic responses (h^E, h^A respectively) of the detector.

$$p_i(t) = h^E_i(t) \times h^A_i(\vec{r}_0, t) \quad (4)$$

The pressure signal when time-reversed is given as

$$p_i(T - t) = h^E_i(T - t) \times h^A_i(\vec{r}_0, T - t) \quad (5)$$

The pressure field at $\vec{r}_0$ generated due to the ith transducer can be given as the convolution of the combined electrical and acoustic responses with the time-reversed pressure signal, that is,

$$p(\vec{r}_0, t) = h^E_i(T-t) \times h^A_i(\vec{r}_0, T-t) \\ \times h^E_i(t) \times h^A_i(\vec{r}_0, t) \qquad (6)$$

The total pressure field due to the contribution from the time-reversed fields transmitted by all the (say total N) transducers is thus expressed as

$$p(\vec{r}_0, t) = \sum_{i=1}^{N} h^E_i(T-t) \times h^A_i(\vec{r}_0, T-t) \\ \times h^E_i(t) \times h^A_i(\vec{r}_0, t) \qquad (7)$$

The time-reversed acoustic fields at $\vec{r}_0$ due to each of the transducers attain their maximum at t = T, thus constructively interfering to produce focused US field at $\vec{r}_0$. Since this is true for an arbitrarily chosen location $\vec{r}_0$, the idea as demonstrated in Figure 2, can be extended to focus the transmitted US signals from the transducers onto the initial pressure source map $H(\vec{r})$ at time t = T.[44]

Therapeutic ultrasonic transducers are capable of transmitting powerful US waves (~MPa) which can cause the rupturing of the blood vessels.[45,46] In Reference 46, a 5 MHz (central frequency) ultrasonic transducer was demonstrated to facilitate PA imaging as well as HIFU treatment where intense US is deposited in the soft tissue and the absorbed energy causes a quick temperature rise afflicting significant damage to the vasculature in the targeted volume. In, Vu et al.[47] reported observing rupturing of blood vessels in mice with ~12 MPa pressure created at a focal volume using HIFU. Similar pressure ranges were reported by Kim et al.[48] for rupturing the blood vessels in earthworms and for porcine femoral arteries by Hoerig et al.[49] and Zhou et al.[50]

While in principle, the concept of time-reversal holds for acoustically non-attenuating media, it does reasonably well for weakly absorbing soft-tissue-like media. Additional sources for inaccuracies in time-reversed fields are finite detection bandwidth and size, detector spacing, and limited-view availability for US collection whose effect will be demonstrated in this paper.

NUMERICAL STUDIES

Numerical studies were performed in two- and three-dimensions using the k-wave toolbox[51] to demonstrate the feasibility of time-reversal guided US treatment of PWS.

Simulations in two-dimensions

Two phantoms mimicking a blood vessel network (of different sizes as shown in Figure 3A,B have been chosen as the pressure sources following absorption of the optical energy from a pulsed laser with ~550−600 nm wavelength which is predominantly absorbed by hemoglobin in PWS blood vessels. Assuming a uniform illumination of the considered structure, a fluence of ~1.5 mJ/cm^2 and blood absorption coefficient of ~350/cm yields 500 mJ/cm^3 of absorbed energy density.[43,52] This leads to ~1 bar rise in the local pressure inside the blood vessel. For setting up the simulation in the k-wave toolbox, the region of interest is considered as a square with side length of 11 cm. For the studies carried out with phantom 1, the computation region was discretized into 472×472 regular grid points with h ~0.23 mm grid resolution. This grid resolution supports the maximum frequency of $v/2h$ ~3.22 MHz for field propagation. The pressure signals were collected at 20 MHz sampling frequency (satisfying the Nyquist criterion[53]: $f_s \geq 2f_{max}$) for 75 microseconds. Owing to the thinner structures, for simulations with phantom 2, the grid resolution was chosen to be ~0.12 mm and the
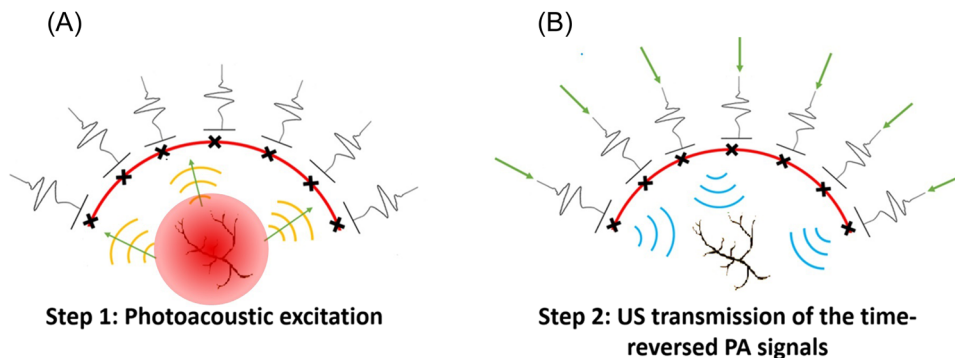
FIGURE 2 Schematic of PA-guided US focusing for PWS treatment depicting (A) photoacoustic excitation and (B) US transmission of the time-reversed PA signal. PA, photoacoustic; PWS, port wine stain; US, ultrasound.
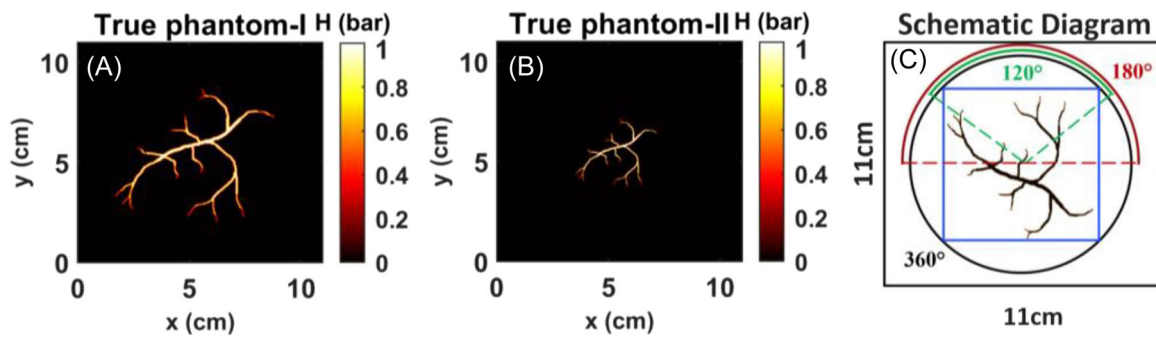
FIGURE 3 (A) True phantom-I, (B) true phantom-II, and (C) the schematic diagram of demonstrating the full and limited-view geometries
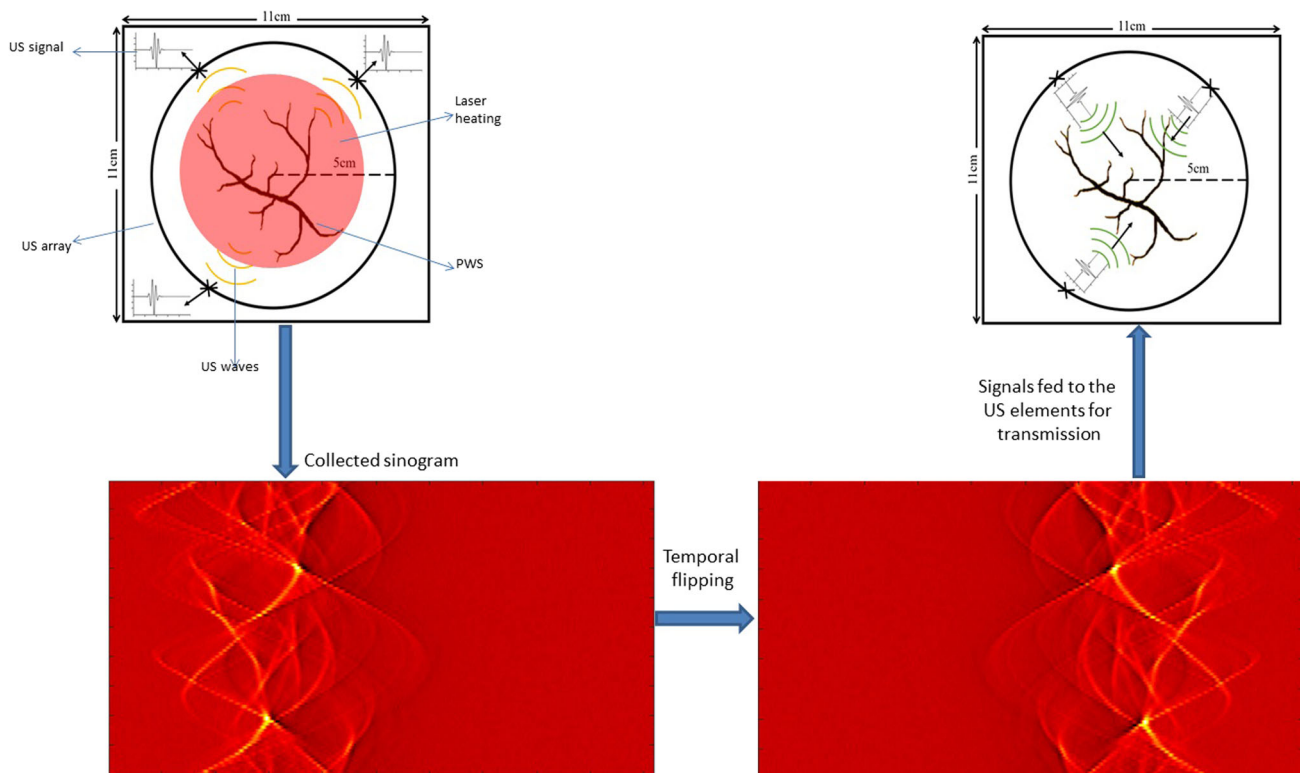

FIGURE 4 Schematic diagram demonstrating the proposed treatment procedure

sampling frequency was chosen to be 40 MHz. In all the simulations, the blood vessel phantom was placed at the center of the computational domain. The speed of sound throughout the medium was chosen as $v = 1500$ m/s. The blood vessel region was surrounded by a number of detectors placed on a circle with 5 cm radius. The number of transducers as well as the collection coverage angles and transducer bandwidths were varied to study their effect on the converging time-reversed fields. The schematic demonstrating the numerical simulation (PA excitation and time-reversal guided US focusing) is shown in Figure 4. We also incorporated the frequency dependent acoustic attenuation of the fields while propagating in the soft tissue which follows the frequency power law given as[54,55]:

$$\alpha(\omega) = \alpha_0 \omega^y \qquad (8)$$

Where $\alpha(\omega)$ denotes the acoustic attenuation (unit: dB/m) at the angular frequency ω (unit: rad/s), α_0 is the power law prefactor (unit: dB (rad/s)$^{-y}$ m^{-1}) with y being the power law exponent (typically $1 \le y \le 2$ in soft tissue). In our work, we have used $y = 1.5$ and $\alpha_0 = 0.5$ dB (rad/s)$^{-1.5}$ m^{-1},[54,55] consistent with the acousto-mechanical properties of human tissue.

The effect of acoustic attenuation on the broadband PA signals generated by phantom 1 and 2 is demonstrated in Figure 5. As evident from Equation 2, a positive value of the power law exponent y means the higher frequency components of the PA signals will be attenuated more as compared to the lower frequency

Effect of the acoustic attenuation on the signal in frequency and time domain
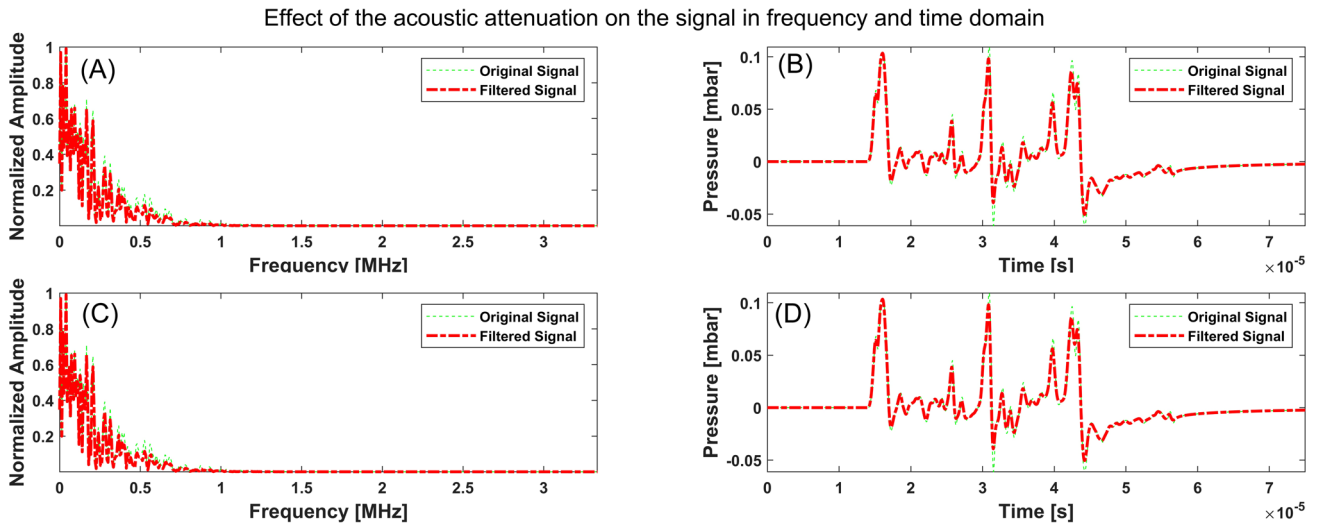
FIGURE 5 Effect of acoustic attenuation on the PA signals: Attenuated (dashed red) and unattenuated (green dots) (A, C) frequency-domain and (B, D) time-domain signals generated from phantom 1 and 2, respectively. PA, photoacoustic.

ones. The thickness of the structures in the blood vessel in phantom 1 is larger than those in phantom 2. Therefore, while the frequency content of phantom 1 is limited to ~0.75 MHz, it extends to ~3 MHz for phantom 2. Since higher acoustic frequencies are more attenuated in the tissue, the difference between the amplitudes of the original and attenuated time-domain PA signals is more significant for phantom 2 as compared to phantom 1.

To model the finite transducer shape and directivity, each of the transducer elements was divided into multiple subdetection points and the detected signal at the element is considered as the weighted average of the signals collected at subdetection points. We employed the Gaussian apodization for computing the weighted average[43]:

$$p(\vec{r_S}, t) = \int_S p(\vec{r}, t) W(\vec{r}) d\vec{r} \qquad (9)$$

Where $p(\vec{r_S}, t)$ denotes the pressure field recorded by a detector centered at $\vec{r_S}$, $p(\vec{r}, t)$ is the pressure field at a location $\vec{r}$ (on the surface of detector S), and $W(\vec{r})$ represents the Gaussian weights. The transducer apodization is considered while sensing as well as transmitting the US signals.

Once the transducers are fully defined, the detection simulation is run by calling the function "*kspaceFirstOrder2D*," the modeled signals are then contaminated with white Gaussian noise to achieve 2 dB SNR. The simulated PA signals are broadband and have frequency components from 0 to $f_s/2$; f_s being the sampling frequency. However, the detection system is typically bandlimited and for an accurate experimental realization, the simulated PA signals are convolved with the transducer's frequency response mimicked as a Gaussian characterized by the central frequency and −6 dB bandwidth. In our simulations, this

has been performed using the "*gaussianFilter*" from the toolbox.

After the (simulated) PA signals were collected at each of the transducers, the transducers were then switched to the transmission mode, that is, each transducer acts as a temporally varying pressure source. Each transducer was modeled to transmit the time-reversed (temporally flipped) PA signal it collected and the temporal evolution of these pressure fields was observed to converge to the PWS model blood vessel. The linearity of the acoustic propagation equation implies that higher pressure strengths in the PWS can be achieved by simply amplifying the US signals transmitted by the transducers.

PWSs typically affect the head and neck,[52] where collection of PA signals all around the region of interest is not feasible. Therefore, simulations have also been performed to study the efficacy of the treatment method with limited collection—transmission views—180° and 120,° as depicted in Figure 3C.

Simulations in three-dimensions

To demonstrate the feasibility of the proposed treatment methodology in a clinically more relevant scenario, we performed a three dimensional simulation using the k-wave toolbox for PA-guided US focusing using a 5×5 cm planar transducer array containing 400 transducer elements for treating three vascular structures. The geometry and the phantom are depicted in Figure 6. For performing the simulation, the computation domain was discretized into $256 \times 256 \times 216$ regular grid points with h ~0.2 mm grid resolution. This grid resolution supports the maximum frequency of $v/2h$ ~3.75 MHz for field propagation. The pressure signals were collected at 20 MHz sampling frequency (satisfying the Nyquist
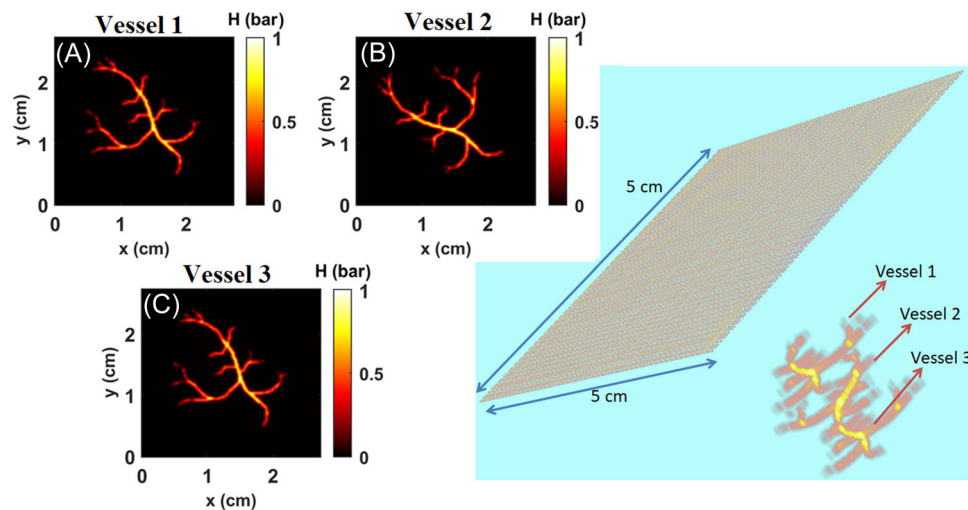
FIGURE 6 xy cross-sections of the true phantoms showing blood vessels (A) vessel 1, (B) vessel 2, and (C) vessel 3. (D) Planar geometry showing the 5×5 cm transducer grid and the relative location of the vascular structures.

criterion[53]: $f_s \geq 2f_{max}$) for 50 microseconds. The 5×5 cm planar transducer grid was divided uniformly into 400 transducer elements, with the size of each element being 0.25×0.25 cm. As in the 2D simulations, to incorporate the finite detector size and directivity, each transducer element was divided into multiple subdetection points and the Gaussian apodization based weighted average (Equation [9]) of the signals collected at subdetection points was considered as the measured signal. The pressure is the vascular structure and other simulation parameters pertaining to the acoustic attenuation, sound speed, transducer bandwidths, and so forth were kept the same as for the 2D simulations. To compare the effect of the transducer aperture size on the US focusing, we also performed a simulation with 0.05×0.05 cm transducer elements uniformly spread on the 5×5 cm planar transducer array with 0.5 mm spacing.

RESULTS AND DISCUSSION

Results: Simulations in two-dimensions

The PA signals in the 2D simulations were collected by the transducers for $T = 75$ microseconds. As discussed in Section 2, the PA signals when time-reversed and transmitted from each element of the transducer grid, converge on to the blood vessel. The temporal evolution of the US signals emitted by the transducers is depicted for phantom 1 in Figure 7 for 128 elements ($f_c = 0.5$ MHz, 80% bandwidth), full-view circular array. Spacing between two consecutive transducers also governs the performance of the proposed method. As demonstrated in Figure 7, the US waves emitted from the transducers converge onto the whole blood vessel when 128 element grid is employed (Figure 8A,D). However, when the

number of elements is reduced to 64, the central parts of the blood vessel receive higher US energy as compared to its branches far from the center (Figure 8B,E). When the number of elements on the grid is further reduced to 32, the US waves converge onto an approximately ~2 cm region of the blood vessel (Figure 8C,F). The off-center branches receive lower US and US energy radiates to the neighboring tissue. Therefore, to treat the PWS, higher number of elements is desired on the transducer grid. This will improve the focusing of the transmitted US waves onto the target blood vessels.

Placing transducers all around the diseased tissue may not be possible as PWSs are commonly located on the head and neck. Moreover, in several scenarios, the path of US propagation is hindered by bones that the US cannot penetrate through.[56] In such cases, the US grid has limited-view/coverage. Simulations have been performed to study the effect of the limited-view on the focusing of the transmitted US waves. Figure 9 demonstrates the US focusing for full-view (128 elements, 360°), half-view (65 elements, 180°), and one-third-view (44 elements, 120°) settings with fixed spacing between elements. As expected, the transmitted US converges best on the blood vessel in the full-view setting (Figure 9A,D). For the limited-view settings, the US is weakly focused on the off-center branches of the blood vessels as shown in Figure 9B−F. Focusing is particularly poor for the structures oriented perpendicular to the transducer surface for the limited-view cases.

Another important factor to govern the efficacy of the proposed methodology is the bandwidth or the frequency response of the transducers. While the PA waves generated due to absorption of a short laser pulse have broadband frequency spectra (100 kHz to 10s of MHz), the frequency responses of the transducers are bandlimited, resulting in loss of the acoustic energy

Temporal evolution of the US emitted from the transducers
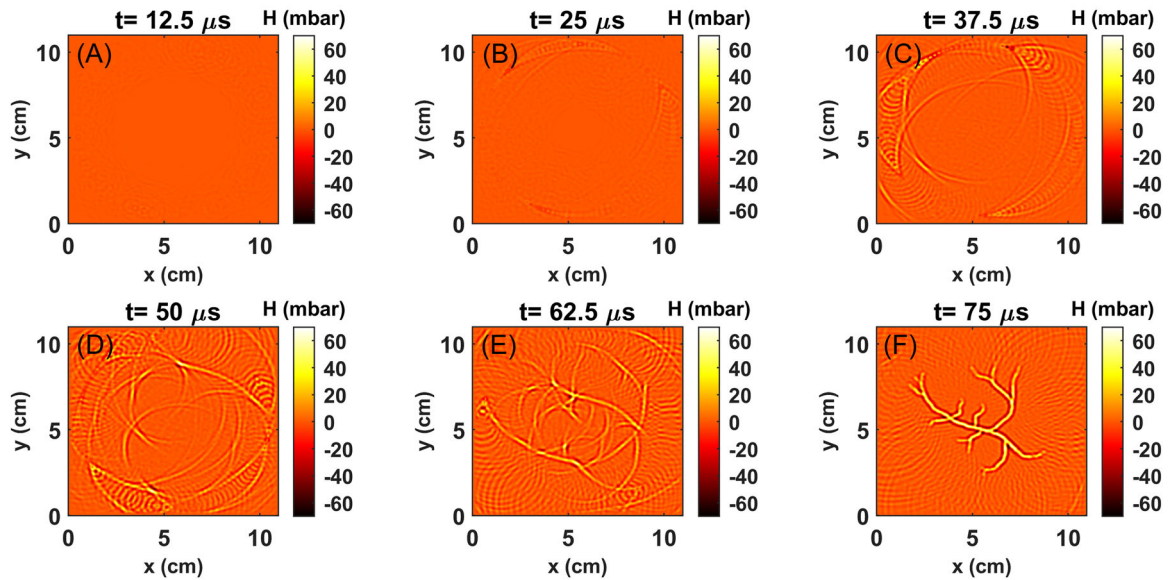
FIGURE 7　Converging US signal to the shape of the blood vessel vasculature. Temporal evolution of ultrasound at (A) 12.5 μs, (B) 25 μs, (C) 37.5 μs, (D) 50 μs, (E) 62.5 μs, and at (F) T = 75 μs converging onto the vasculature (phantom-1). US, ultrasound.
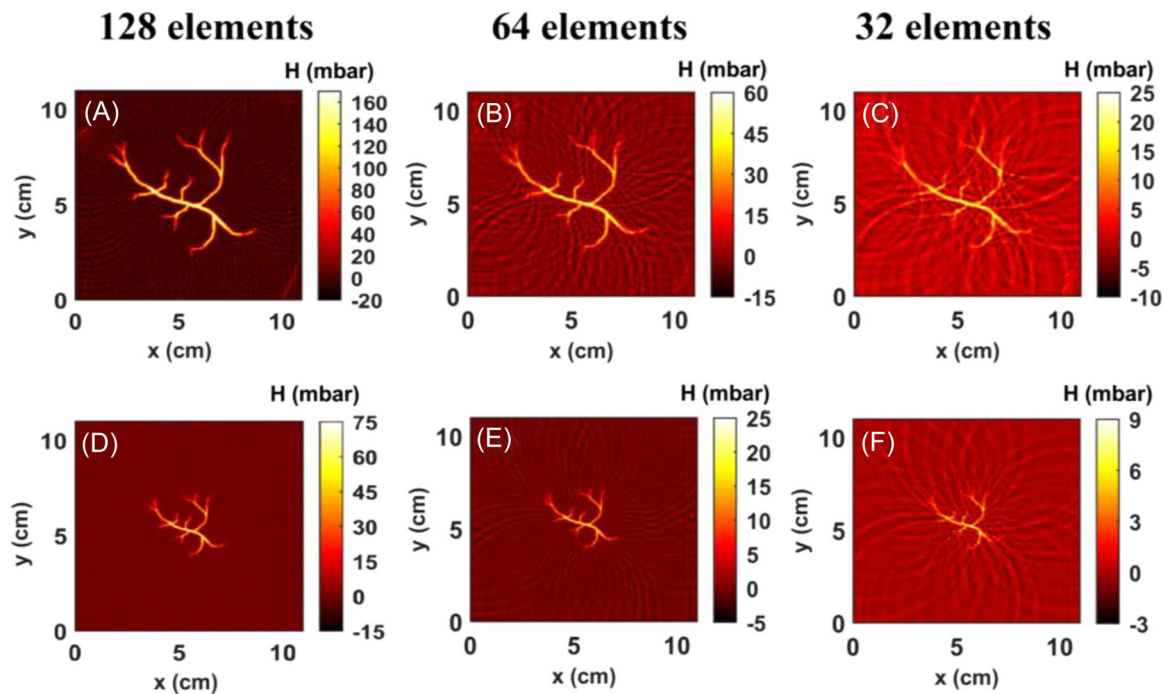
FIGURE 8　Effect of element size on the focused US map: (A–C) phantom-1 and (D–F) phantom 2. US, ultrasound.

collected. Consequently, the magnitude of the focused US on the targeted blood vessel would also be smaller. In this study, we simulated the frequency response as a Gaussian filter with central frequencies (f_c) of 0.5, 1, and 2 MHz, with 80% bandwidth. The effect of detection response on the PA signals is demonstrated in Figures 10 and 11 for phantom 1 and 2, respectively and the

converged US fields at 75 microseconds are displayed in Figure 12.

As expected, the converged US energy is more diffused for the transducers with low central frequency (Figure 12A,D) as compared to the ones with higher central frequencies (Figure 12B–F). As indicated in Figures 10 and 11, the US energy of the true PA signals
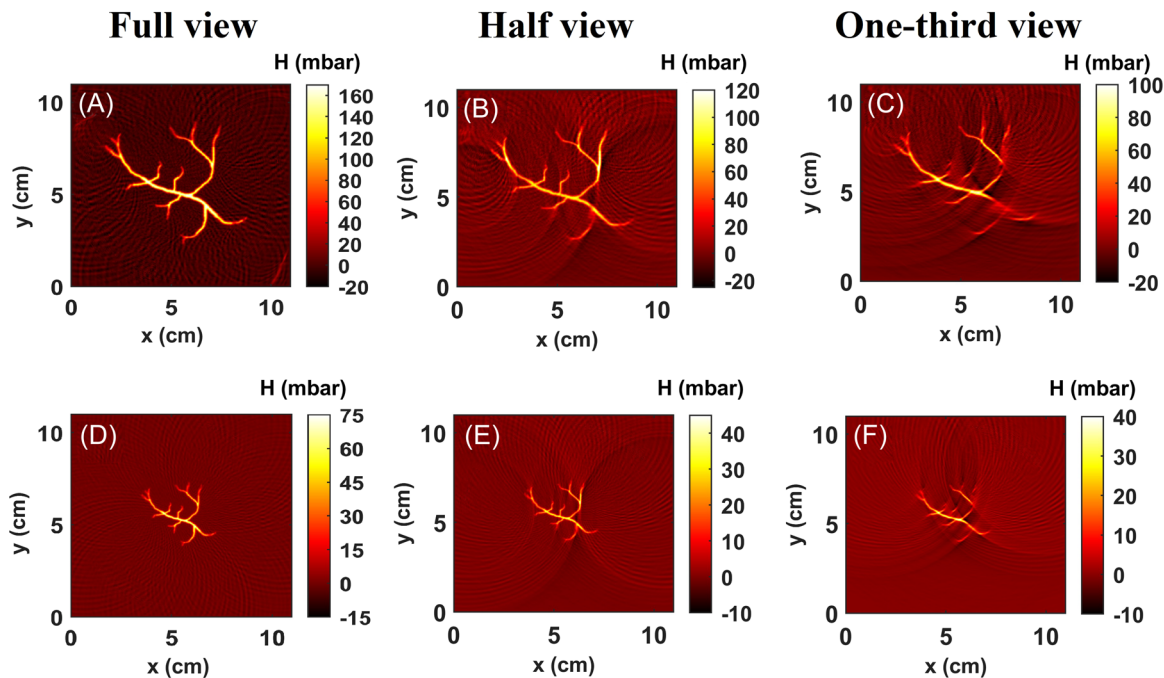
FIGURE 9 Effect of full and partial-views on the converged US field: (A–C) phantom-1 and (D–F) phantom 2. US, ultrasound.
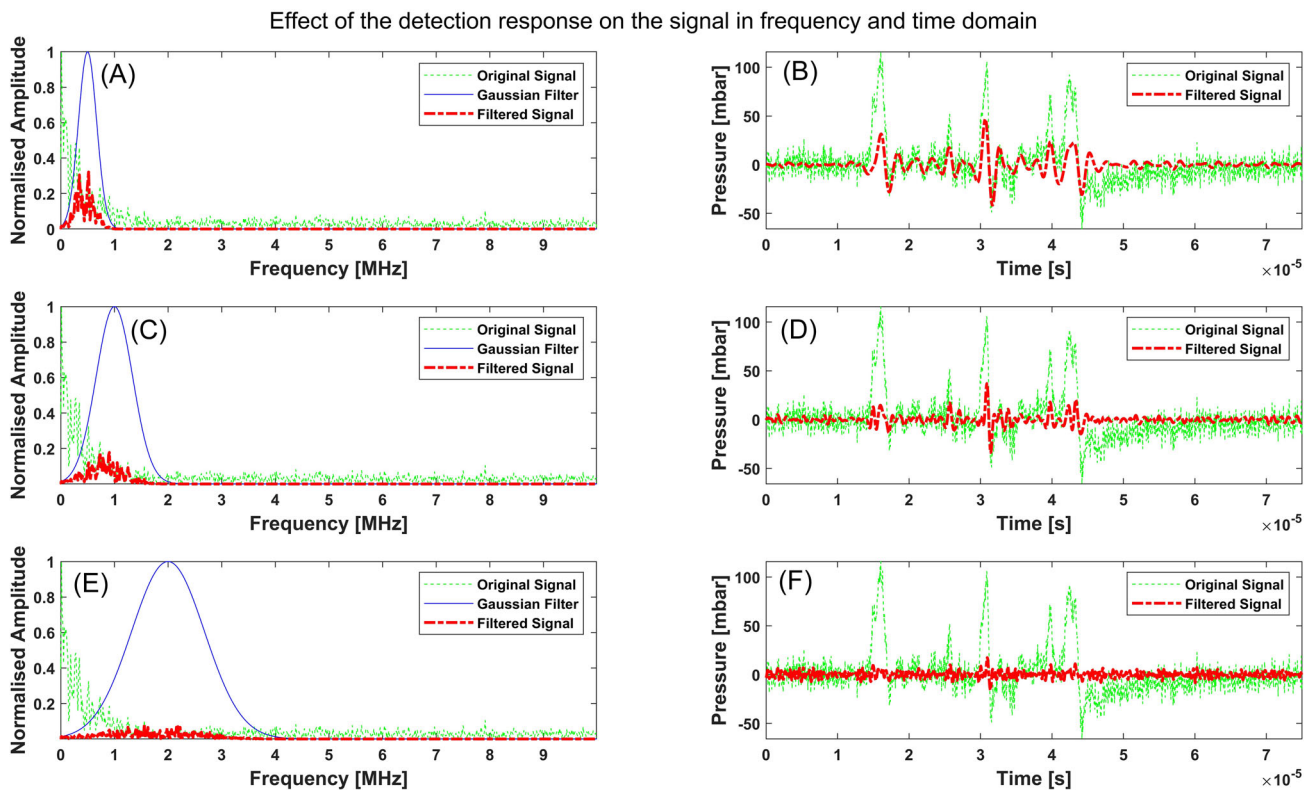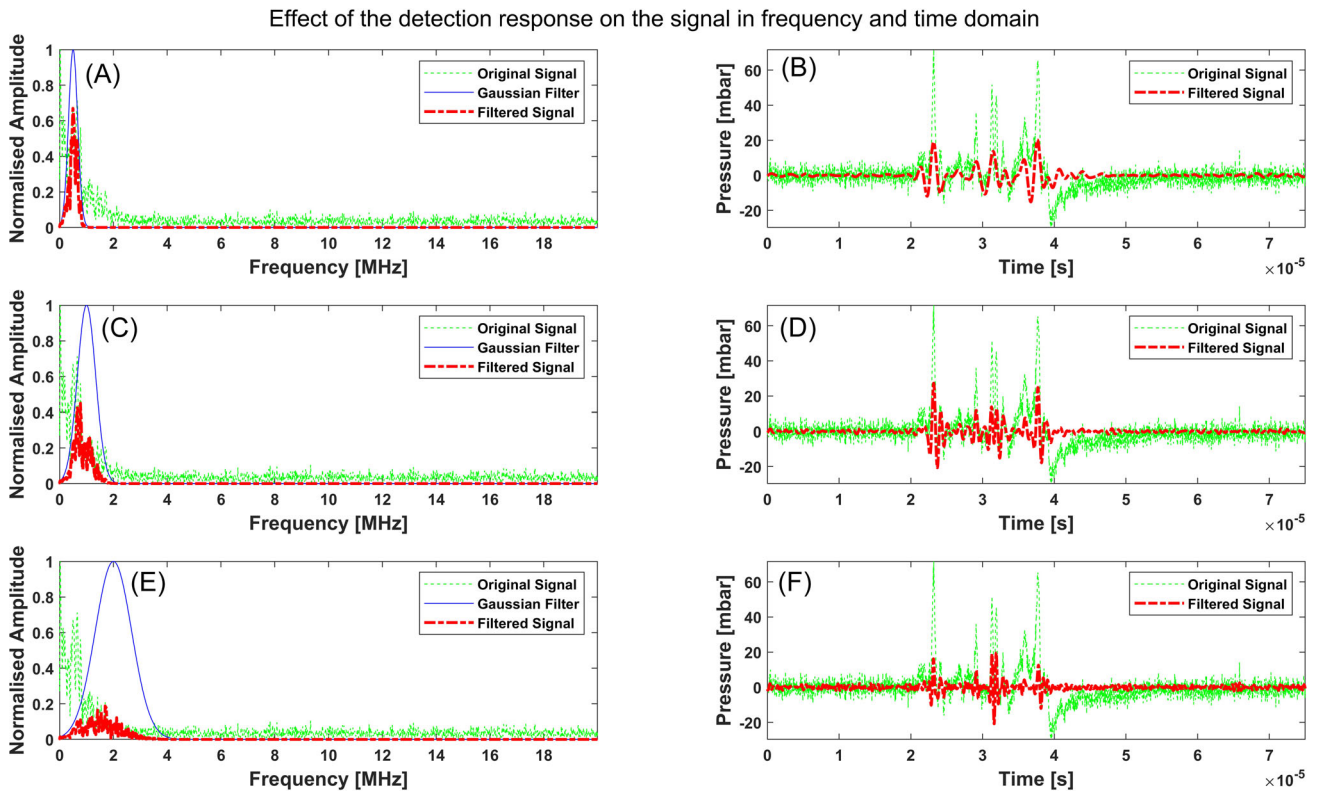

FIGURE 10 Filtering of PA signals from phantom 1. [Phantom-1] Demonstration of the effect of detector response (represented by Gaussian filter) on the photoacoustic signals in the frequency- and time-domain, respectively for (A, B) fc = 0.5 MHz, 80% BW, (C, D) fc = 0.5 MHz, 80% BW, and (E, F) fc = 0.5 MHz, 80% BW. PA, photoacoustic.

Effect of the detection response on the signal in frequency and time domain

FIGURE 11 Filtering of PA signals from phantom 2. [Phantom-2] Demonstration of the effect of detector response (represented by Gaussian filter) on the photoacoustic signals in the frequency- and time-domain, respectively for (A, B) fc = 0.5 MHz, 80% BW, (C, D) fc = 0.5 MHz, 80% BW, and (E, F) fc = 0.5 MHz, 80% BW. PA, photoacoustic
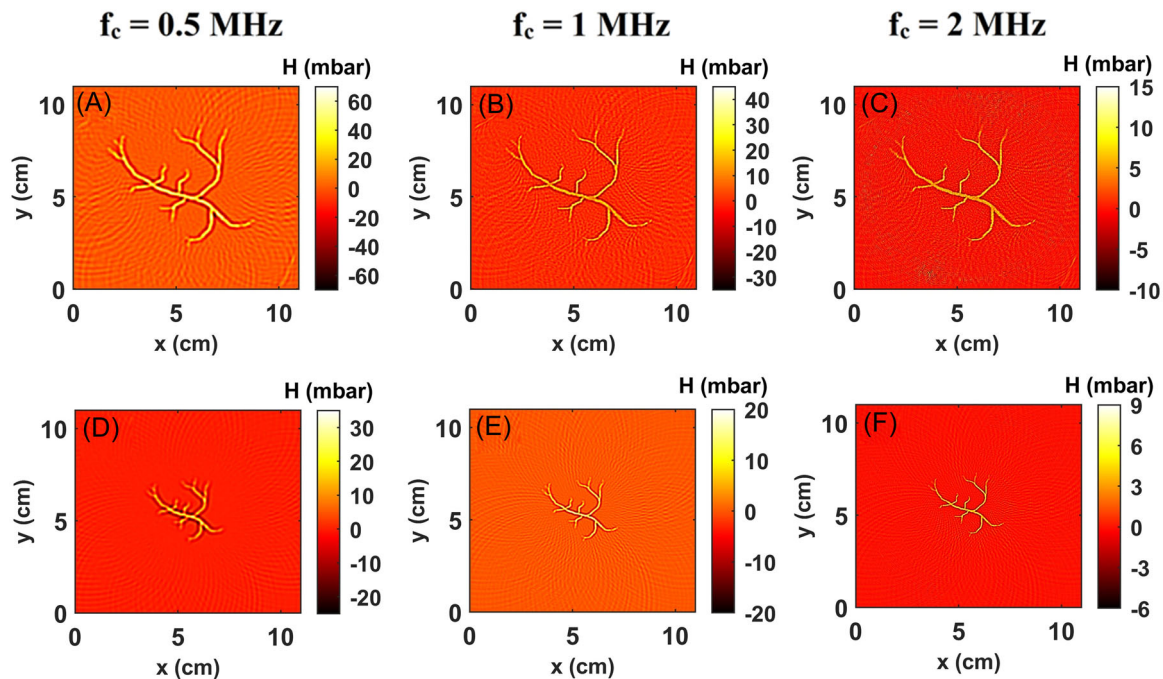

FIGURE 12 US energy distribution obtained from a ring a rray of US transceivers with 80% filter bandwidth and center frequencies of 0.5 MHz, (B, E), 1 MHz, and (C, F) 2 MHz for phantom-1 and phantom-2, respectively. US, ultrasound.

from both the phantoms is primarily concentrated in the lower frequencies. Therefore, the magnitude of the focused US decreases with increasing transducer central frequency for both the phantom as shown in Figure 12. Another factor contributing to this is the acoustic attenuation in the medium, which as per Equation 2, is

stronger for the higher frequencies, thus further reducing the US energy contained in the higher frequency components. Also, the more the US travels in an acoustically attenuating media, the more it will attenuate. Therefore, as compared to phantom 1, the magnitude of the focused US irrespective of the transducer bandwidth,
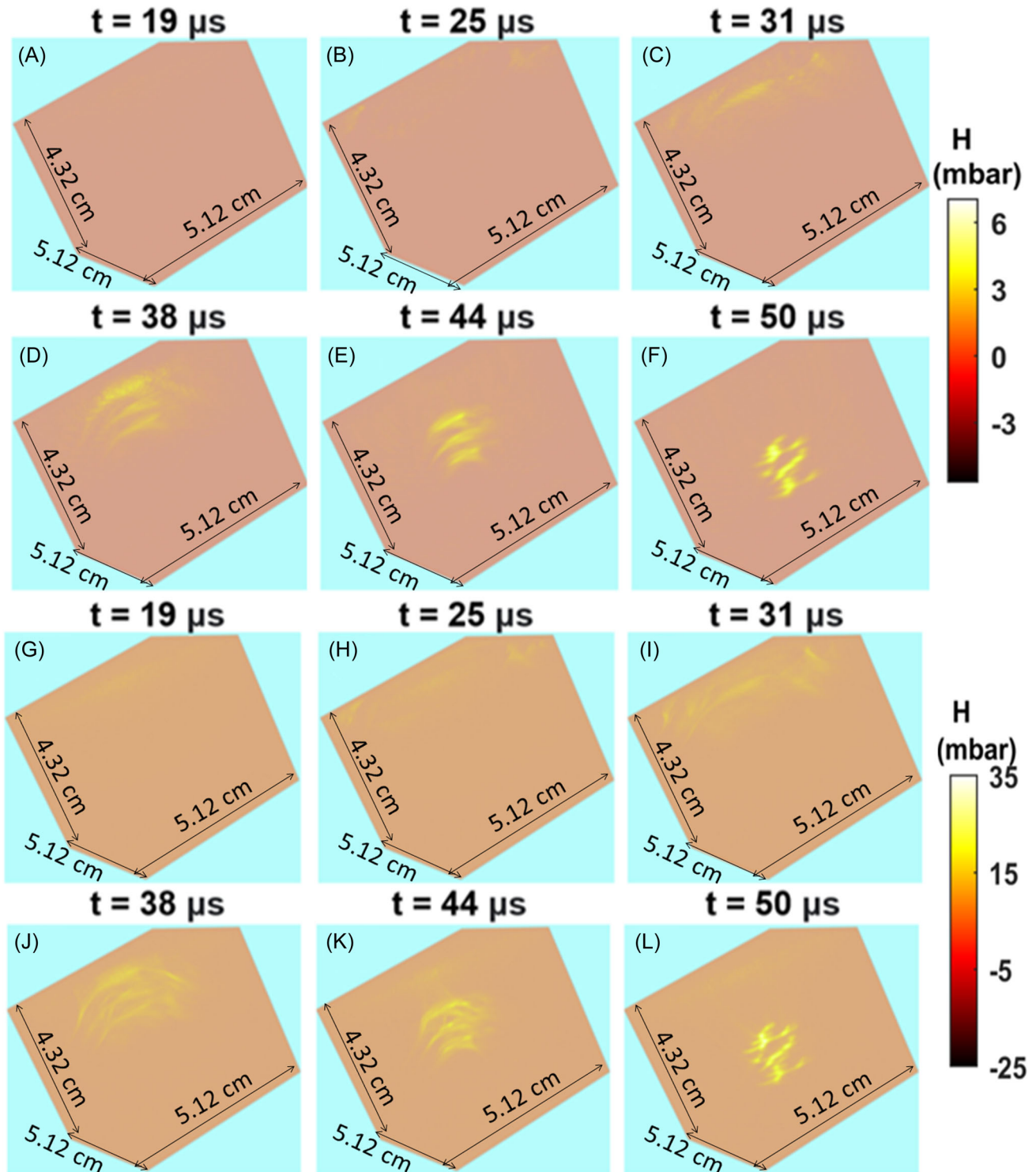
FIGURE 13 Temporal evolution of ultrasound focusing onto the vascular structures at different depths from planar transducer array with (A–F) 400 elements with 0.25 cm element size and (G–L) 10,000 elements with 0.05 cm element size

is weaker for phantom 2, which is located farther from the transducer grid. The choice of the transducer with consideration for an appropriate detection bandwidth is thus critical for the success of PWS treatment with the proposed methodology. The blood vessels are typically thin (~100 μm to 1 mm) yielding high frequency PA signals. However, due to higher acoustic attenuation of the high frequency components, transducers with relatively lower central frequency should be preferred.

Results: Simulations in three-dimensions

The PA signals in the 3D simulations were collected by the transducers for $T = 50$ microseconds. The PA signals when time-reversed and transmitted from each of the transducers converge on to the blood vessel. The temporal evolution of the US emitted from the transducers for 0.25 and 0.05 cm transducer element sizes are shown in Figure 13A−F and Figure 13G−L, respectively. As explained in Section 2, the US waves for both the transducer arrays converge onto the vascular structures at $t = T = 50$ microseconds (the duration for which the PA signals were collected). The focused US maps of the three vascular structures located at different depths from the transducer array for the aforementioned two transducer settings are demonstrated in Figure 14A−C and Figure 14D−F, respectively. As expected, the smaller aperture size of the elements facilitates better focusing. Moreover, the contribution from a higher number of transducers facilitates a higher magnitude of pressure

focused onto the vascular structures. The PA waves originating from the deeper structures undergo higher acoustic attenuation and hence have a lower contribution to the collected PA signals. Moreover, the PA signals when time-reversed and transmitted from the transducers suffer higher acoustic attenuation before reaching the deeper structures. Consequently, for both the transducer settings, the magnitude of the converged pressure onto the vascular structures decreases with distance from the transducer array. The planar transducer arrays considered in this study offer a limited view of PA collection and US transmission. This leads to a weaker focus of the US onto the off-center structures with respect to the coplanar structures which are closer to the center. Therefore, a large transducer array with high transducer element density should be more effective in treating PWS (as concluded from the 2D simulations as well); however, the size is always going to be limited based on the access to the PWS site and the elemental density is expected to have limitations due to manufacturing and cost constraints.

In pulsed dye laser based PWS treatment (current clinical methodology), vessels higher in the dermis absorb the majority of the light and prevent effect in vessels underneath because of the high optical attenuation (absorption + scattering losses) in the soft tissue. Once a vessel is coagulated it can slowly be resorbed but there is also revascularization or angiogenesis that can occur.[57] In the proposed methodology however, owing to low US attenuation in soft tissues, the US energy is focused onto the vessels at multiple depths. While the focused
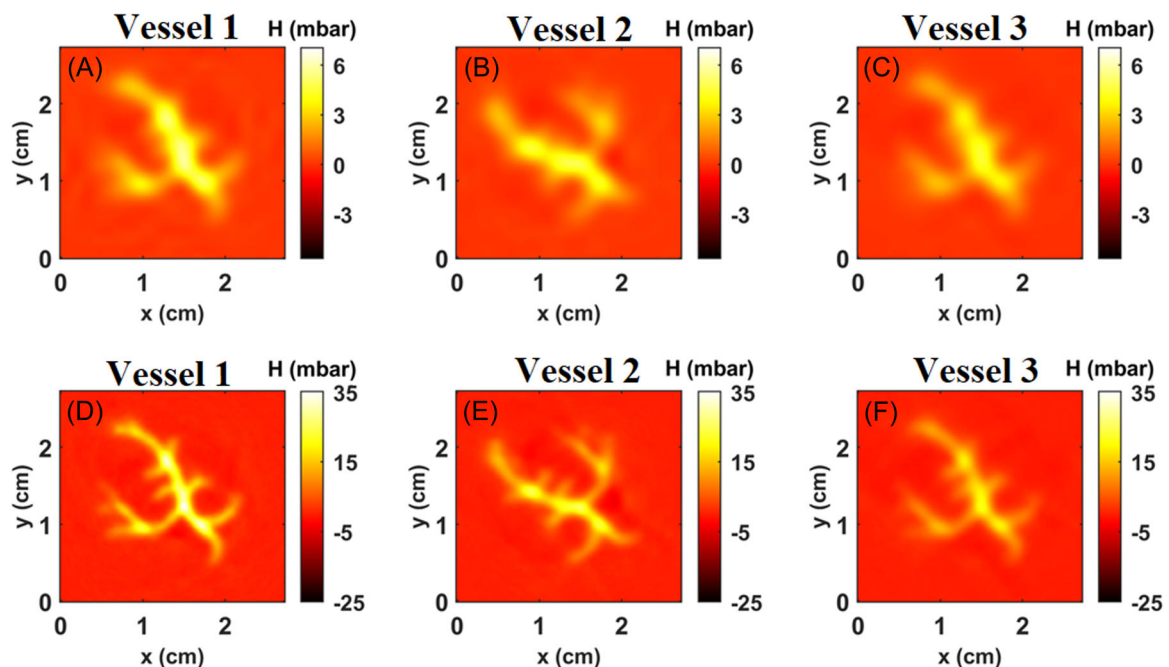
FIGURE 14 Converged US on to the vascular structures at different distances from the transducer array with (A−C) 400 elements with 0.25 cm element size and (D−F) 10,000 elements with 0.05 cm element size. US, ultrasound.

pressure amplitudes do decrease with the depth in the tissue, the decrement is much smaller as compared to that of light as indicated in Figure 14 of the manuscript.

Moreover, the PA signals originating from the destroyed superficial vessels can be differentiated from the signals from deeper vessels based on the time of flight information. The contribution to the PA signals originating from the destroyed superficial blood vessels can then be ameliorated before the signals are time-reversed, amplified, and transmitted from the transducers.

The computational studies in this study demonstrate the methodology and the efficacy of time-reversal guided US focusing for noninvasive PWS birthmarks treatment with minimal effect on neighboring tissue. The proposed strategy could also benefit existing methodologies for US sonication which use microbubbles for rupturing blood vessels[35,36] and for improved permeability for intravascular delivery of gene therapy and medications.[37] The methodology can also assist other targeted US therapeutic techniques aiming awound healing and cancer therapy.[38–41] While the simulations presented in this paper are proof of the concept studies, the efficacy of PWS treatment using the proposed methodology needs to be experimentally and clinically evaluated and will be the focus of our future research.

CONCLUSION

The urrent standard of care pulsed dye laser-based treatment for port-wine stains is achieved by high-intensity laser excitation and subsequent thrombosis and destruction of blood vessels. However, in the process, a significant amount of optical energy is absorbed in the skin and the neighboring tissues which may be painful and cause thermal damage. Epidermal cooling methods and anesthesia are required to address these issues. In this paper, we propose a PA-guided US focusing methodology for PWS treatment. It is a novel approach, using US, to target deeper PWS vessels that remain untreated with conventional laser therapy and contribute to treatment resistance. We demonstrate the feasibility of using PA imaging to create an optical absorption map and enable selective US focusing onto the PWS tissue when the US signals are time-reversed, amplified, and transmitted while minimally affecting neighboring tissue. We performed simulations that mimic realistic transducers and medium properties for this proof of concept study demonstrating the feasibility of the proposed methodology. The studies indicate that a high coverage angle and element density of the transducer grid are crucial for achieving better convergence of the US field onto the targeted vessels. High elemental spacing in the detection grid leads to poorly focused US energy deposition on off-center targets and relatively higher energy deposition in neighboring tissue. Moreover, a transducer grid with low coverage angle causes poor US focusing on the blood vessels oriented perpendicular to the grid. Another governing factor for the efficacy of this methodology is choosing the transducer grid with an appropriate detection bandwidth. The submillimeter thick blood vessels produce high-frequency PA signals. However, due to higher acoustic attenuation of the high frequency components, transducers with relatively lower central frequency should be preferred. The presented methodology can also benefit other US therapeutic modalities such as sonication and increasing permeability for drug and gene delivery to blood vessels. Experimental evaluation of the proposed methodology for PWS treatment will be the focus of future clinical translation studies.

ORCID
Prabodh K. Pandey http://orcid.org/0000-0002-8962-2580
Kristen M. Kelly http://orcid.org/0000-0002-5988-2197

REFERENCES
1. Updyke KM, Khachemoune A. Port-wine stains: a focused review on their management. J Drugs Dermatol. 2017;16(11):1145–51.
2. Ortiz AE, Nelson JS. Port-wine stain laser treatments and novel approaches. Facial Plast Surg. 2012;28(6):611–20.
3. McLean P. Family practice: a strategy for survival. Can Fam Physician. 1980;26(6–7):6–7.
4. Kelly KM, Choi B, McFarlane S, Motosue A, Jung B, Khan MH, et al. Description and analysis of treatments for port-wine stain birthmarks. Arch Facial Plast Surg. 2005;7(5):287–94.
5. Anderson RR, Parish JA. Selective photothermolysis: precise microsurgery by selective absorption of pulsed radiation. Science. 1983;220(4596):524–7.
6. Sharif SA, Taydas E, Mazhar A, Rahimian R, Kelly KM, Choi B, et al. Noninvasive clinical assessment of port-wine stain birthmarks using current and future optical imaging technology: a review. Br J Dermatol. 2012;167(6):1215–23.
7. Brightman LA, Geronemus RG, Reddy KK. Laser treatment of port-wine stains. Clin Cosmet Investig Dermatol. 2015;8:27–33.
8. Nelson JS, Milner TE, Anvari B, Tanenbaum BS, Kimel S, Svaasand L, et al. Dynamic epidermal cooling during pulsed laser treatment of port-wine stain. A new methodology with preliminary clinical evaluation. Arch Dermatol. 1995;131(6):695–700.
9. Khandpur S, Sharma VK. Assessment of efficacy of the 595-nm pulsed dye laser in the treatment of facial port-wine stains in Indian patients. Dermatol Surg. 2016;42(6):717–26.

10. Torezan L. Lasers in pigmented skin. Pig Ethnic Skin Imported Derma. 2018;1(47):519–27.

11. Zhao Y, Tu P, Zhou G. Hemoporfin photodynamic therapy for port-wine stain: a randomized controlled trial. PloS. 2016; 11(5):156219.

12. Khalaf AT, Sun Y, Wang F, Sheng M. Photodynamic therapy using HMME for port-wine stains: clinical effectiveness and sonographic appearance. BioMed Res Int. 2020;2020:1–7.

13. Yuan K-H, Li Q, Yu W-L, Huang Z. Photodynamic therapy in treatment of port wine stain birthmarks—recent progress. Photodiagn Photodyn Ther. 2009;6(3):189–94.

14. Zhang L-C, Yang J, Huang Y-B, Huang Z. Post treatment care in photodynamic therapy (PDT) of large facial port-wine stain (PWS) birthmarks. Photodiagn Photodyn Ther. 2021;36(102604):102604.

15. Yuan K-H, Gao J-H, Huang Z. Adverse effects associated with photodynamic therapy (PDT) of port-wine stain (PWS) birthmarks. Photodiagn Photodyn Ther. 2012;9(4):332–336.

16. van Raath MI, Chohan S, Wolkerstorfer A, van der Horst C, Storm G, Heger M. Port wine stain treatment outcomes have not improved over the past three decades. J Eur Acad Dermatol Venereol. 2019;33(7):1369–77.

17. Alkahtani SA, Kunwar PS, Jalilifar M, Rashidi S, Yadollahpour A. Ultrasound-based techniques as alternative treatments for chronic wounds: a comprehensive review of clinical applications. Cureus. 2017;9(12):1952.

18. Yadollahpour A, Jalilifar M, Rashidi S, Rezaee Z. Ultrasound therapy for wound healing: a review of current techniques and mechanisms of action. J Pure Applied Microbiol. 2014;8(5):4071–85.

19. Buch J, Karagaiah P, Raviprakash P, Patil A, Kroumpouzos G, Kassir M, et al. Noninvasive diagnostic techniques of port wine stain. J Cosmet Dermatol. 2021;20(7):2006–14.

20. Troilius A, Svendsen G, Ljunggren B. Ultrasound investigation of port wine stains. Acta Derm-Venereol. 2000;80(3):196–9.

21. Kwiek B, Paluch Ł, Kowalewski C, Ambroziak M. Facial hypertrophic port-wine stain treatment combining large spot 532 nm laser, high-intensity focused ultrasound and traction threads. Dermatol Surg. 2020;46(7):988–90.

22. Bell AG. On the production and reproduction of sound by light. Am J Sci. 1880;s3-20(118):305–24.

23. Attia ABE, Ntziachristos V, Balasundaram G, Moothanchery M, Dinish US, Bi R, et al. A review of clinical photoacoustic imaging: current and future trends. Photoacoustics. 2019;16:100144.

24. Das D, Sharma A, Rajendran P, Pramanik M. Another decade of photoacoustic imaging. Phys Med Biol. 2021;66(5):05TR01.

25. Zhao Y, Wang S, Merrill JA, Arellano JD, Trevisi LM, Li Y, et al. Triplex radiometric, photoacoustic, and ultrasonic imaging based on single-pulse excitation. Opt Lett. 2020;45(7):1703–06.

26. Xiang L, Wang B, Ji L, Jiang H. 4-D photoacoustic tomography. Sci Rep. 2013;3(1):1–8.

27. Kruger RA, Kuzmiak CM, Lam RB, Reinecke DR, Del Rio SP, Steed D. Dedicated 3D photoacoustic breast imaging. Med Phys. 2013;40(11):113301.

28. Yao J, Wang LV. Photoacoustic brain imaging: from microscopic to macroscopic scales. Neurophotonics. 2014;1(1):011003.

29. Wang S, Echeverry J, Trevisi L, Prather K, Xiang L, Liu Y. Ultrahigh resolution pulsed laser-induced photoacoustic detection of multi-scale damage in CFRP composites. Applied Sciences. 2020;10(6):2106.

30. Glorieux C. Perspective on non-invasive and non-destructive photoacoustic and photothermal applications. J Appl Phys. 2022;131(17):170903.

31. Singh MKA, Steenbergen W. Photoacoustic-guided focused ultrasound (PAFUSion) for identifying reflection artifacts in photoacoustic imaging. Photoacoustics. 2015;3(4):123–31.

32. Singh MKA, Jaeger M, Frenz M. In vivo demonstration of reflection artifact reduction in photoacoustic imaging using synthetic aperture photoacoustic-guided focused ultrasound (PAFUSion). Biomed Opt Express. 2016;7(8):2955–72.

33. Prost A, Funke A, Tanter M. Photoacoustic-guided ultrasound therapy with a dual-mode ultrasound array. J Biomed Opt. 2012;17(6):061205.

34. Doucette K, O'Malley J, White P. A novel application of focused ultrasound for the treatment of port wine stain birthmarks. NLM. 2019;2019(1):G70–072.

35. Hosseinkhah N, Chen H, Matula TJ. Mechanisms of microbubble–vessel interactions and induced stresses: a numerical study. J Acoust Soc Am. 2013;134(3):1875–85.

36. Singh R, Jo J, Riegel M. The feasibility of ultrasound-assisted endovascular laser thrombolysis in an acute rabbit thrombosis model. Med Phys. 2021;48(8):4128–38.

37. Lin CY, Tseng HC, Shiu HR. Ultrasound sonication with microbubbles disrupts blood vessels and enhances tumor treatments of anticancer nanodrug. Int J Nanomedicine. 2012;7:2143–52.

38. Lai P, Tarapacki C, Tran W. Breast tumor response to ultrasound mediated excitation of microbubbles and radiation therapy in vivo. Oncoscience. 2016;3(3–4):98–108.

39. Ho YJ, Chu SW, Liao EC. Normalization of tumor vasculature by oxygen microbubbles with ultrasound. Theranostics. 2019; 9(24):7370–83.

40. Wood AKW, Sehgal CM. A review of low-intensity ultrasound for cancer therapy. Ultrasound Med Biol. 2015;41(4):905–28.

41. ter Haar G. Therapeutic applications of ultrasound. Prog Biophys Mol Biol. 2007;93(1–3):111–29.

42. Wang LV, Wu H-I. Biomedical Optics: Principles and Imaging. John Wiley & Sons; 2012.

43. Warbal P, Pramanik M, Saha R. Impact of sensor apodization on the tangential resolution in photoacoustic tomography. J Optical Soc Am. 2019;36(2):245–52.

44. Fink M. Time reversal of ultrasonic fields. I. Basic principles. IEEE Trans Ultrason Eng. 1992;39(5):555–66.

45. Shaw CJ, Ter Haar GR, Rivens IH, Giussani DA, Lees CC. Pathophysiological mechanisms of high-intensity focused ultrasound-mediated vascular occlusion and relevance to non-invasive fetal surgery. J R Soc Interface. 2014;11(95):20140029.

46. Cui H, Staley J, Yang X. Integration of photoacoustic imaging and high-intensity focused ultrasound. J Biomed Opt. 2010;15(2):021312.

47. Vu T, Tang Y, Li M, Sankin G, Tang S, Chen S, et al. Photoacoustic computed tomography of mechanical HIFU-induced vascular injury. Biomed Opt Express. 2021;12(9):5489–98.

48. Kim Y, Nabili M, Acharya P, Lopez A, Myers MR. Microvessel rupture induced by high-intensity therapeutic ultrasound—a study of parameter sensitivity in a simple in vivo model. J Ther Ultrasound. 2017;5(1):1–9.

49. Hoerig CL, Serrone JC, Burgess MT, Zuccarello M, Mast TD. Prediction and suppression of HIFU-induced vessel rupture using passive cavitation detection in an ex vivo model. J Ther Ultrasound. 2014;2(1):1–18.

50. Zhou Y, Lim WCD. Influence of high-intensity focused ultrasound (HIFU) ablation on arteries: ex vivo studies. Micromachines. 2021;12(5):485.

51. Treeby BE, Cox BT. K-wave: MATLAB toolbox for the simulation and reconstruction of photoacoustic wave fields. J Biomed Opt. 2010;15(2):021314.

52. Keijzer M, Pickering JW, Gemert MJ. Laser beam diameter for port wine stain treatment. Lasers Surg Med. 1991;11(6):601–605.

53. Oppenheim AV, Schafer RW, Buck JR. Discrete Time Signal Processing. Prentice hall; 2001.

54. Ammari H, Bretin E, Jugnon V. Photoacoustic imaging for attenuating acoustic media. Mathematical Modeling in Bio-medical Imaging II. Springer; 2012. p. 57–84.

55. Treeby BE. Acoustic attenuation compensation in photoacoustic tomography using time-variant filtering. J Biomed Opt. 2013;18(3):036008.

56. Smith J, Finnoff JT. Diagnostic and interventional musculo-skeletal ultrasound: part 1. Fundamentals. PM & R: J Injury, Function, Rehab. 2009;1(1):64–75.

57. Choi B, Jia W, Channual J, Kelly KM, Lotfi J. The importance of long-term monitoring to evaluate the microvascular response to light-based therapies. J Invest Dermatol. 2008;128(2):485–8.

SUPPORTING INFORMATION

Additional supporting information can be found online in the Supporting Information section at the end of this article.